

EFFECT OF UPSTREAM FLOW CONDITIONS ON ACOUSTIC FEEDBACK-LOOP INTERACTIONS IN TRANSITIONAL AIRFOILS

VLADIMIR V. GOLUBEV^{*}, LAP NGUYEN^{*}, SAM SALEHIAN^{*},
REDA R. MANKBADI^{*} AND MICHEL ROGER[†]

^{*} Florida Center for Advanced Aero Propulsion
Department of Aerospace Engineering
Embry-Riddle Aeronautical University
Daytona Beach, FL 32127, USA
e-mail: Vladimir.Golubev@erau.edu

[†] Laboratoire de Mécanique des Fluides et d'Acoustique
Ecole Centrale de Lyon
Ecully 69134, France
email: Michel.Roger@ec-lyon

Key Words: *ILES, Transitional Airfoil, Flow-Acoustic Interactions, Synthetic Turbulence*

Abstract. Reported high-accuracy numerical experiments focus on examining upstream turbulence effects on flow-acoustic resonant interactions observed for transitional airfoils at moderate Reynolds numbers. A novel highly efficient approach is employed to generate a three-dimensional, divergence-free, convected turbulent velocity field with prescribed integral characteristics by means of a time-dependent momentum source located in an arbitrary region of the computational domain upstream of a solid body. The results of parametric studies indicate the effects of increasing turbulence intensity on the airfoil boundary-layer statistical moments and related unsteady aerodynamic and acoustic responses.

1 INTRODUCTION

The current paper examines effects of upstream unsteady flow conditions on the acoustic feedback-loop mechanism of flow-acoustic resonant interactions observed in transitional airfoil boundary layers at certain flow regimes (Fig. 1). In our previous works [1-3], experimentally recorded unsteady responses of loaded, transitional NACA0012 airfoil confirmed the presence of the shifted ladder-type tonal structures with dual velocity dependence first observed in the acoustic signals by Paterson et al [4]. The current paper extends the previous numerical studies by focusing on the sensitivity of the airfoil flow-acoustic interactions (and the resulting acoustic signature) to the upstream unsteady flow conditions. In particular, we consider the effect of upstream turbulence, with the analysis employing a recently developed novel numerical procedure [5-6].

Section 2 discusses the high-fidelity numerical approach that employs a 6th-order Navier-Stokes solver implementing a low-pass filtering of poorly resolved high-frequency solution

content to retain numerical accuracy and stability over the range of transitional flow regimes.

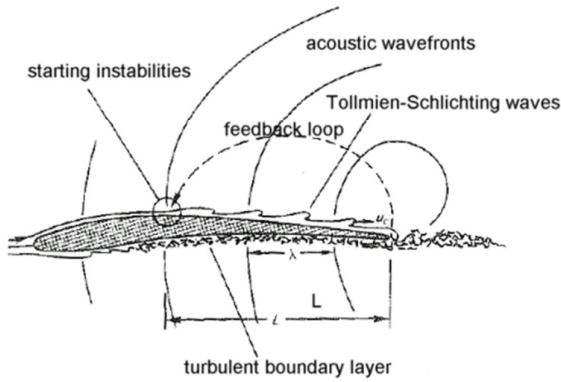


Figure 1: Feedback loop in airfoil flow-acoustic interactions.

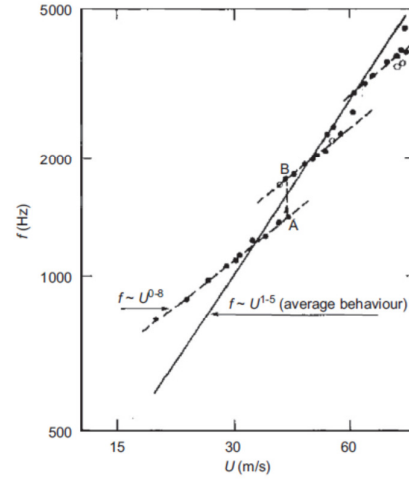


Figure 2: Airfoil ladder-type frequency structure, from Paterson et al. [4].

For the purpose of the present study, Section 3 provides an overview of the developed approach [5-6] to generate an upstream synthetic turbulent velocity field in a specified source region upstream of the airfoil. Such method essentially extends our previously developed technique [7] to generate a divergence-free time-harmonic vortical gust. The resulting analytical procedure to generate an arbitrary velocity field through superposition of Fourier harmonics blends particularly well with the spectral method originally outlined by Kraichnan [8], developed into a random flow generation procedure for anisotropic turbulence by Smirnov et al [9], and further elaborated for hybrid RANS/LES methods by Batten et al. [10].

Finally, Section 4 focuses on the results of 2D numerical experiments investigating the effect of upstream turbulence on the unsteady aerodynamic and acoustic responses of a transitional airfoil exhibiting a complex phenomenon of boundary-layer flow-acoustic resonant interactions. Such phenomenon is characterized by the presence of separation regions and the resulting formation of the highly-amplified instability waves scattered into noise at the airfoil trailing edge, thus triggering and sustaining the acoustic feedback-loop process. The disruption of the feedback mechanism introduced by the impinging upstream turbulence characterized by different intensity levels is the subject of the conducted parametric studies.

2 GOVERNING EQUATIONS

All numerical simulations presented in the current work employ a high-fidelity numerical code [11] solving a set of compressible Navier-Stokes equations represented in strong, conservative, time-dependent form in the generalized curvilinear computational coordinates (ξ, η, ζ, τ) transformed from the physical coordinates (x, y, z, t) :

$$\frac{\partial}{\partial \tau} \left(\frac{\vec{Q}}{J} \right) + \frac{\partial \vec{F}_i}{\partial \xi} + \frac{\partial \vec{G}_i}{\partial \eta} + \frac{\partial \vec{H}_i}{\partial \zeta} + \frac{1}{Re} \left[\frac{\partial \vec{F}_v}{\partial \xi} + \frac{\partial \vec{G}_v}{\partial \eta} + \frac{\partial \vec{H}_v}{\partial \zeta} \right] = \vec{S} \quad (1)$$

The solution vector $\vec{Q} = \{\rho, \rho u, \rho v, \rho w, \rho e\}$ is defined in terms of the flow density ρ , Cartesian flow velocity components (u, v, w), and flow specific energy,

$$e = \frac{T}{\gamma(\gamma - 1)M_\infty^2} + \frac{1}{2}(u^2 + v^2 + w^2) \quad (2)$$

with assumed perfect gas relationship $p = \rho T / \gamma M_\infty^2$ connecting the flow pressure p , temperature T , and the freestream Mach number M_∞ (γ is the specific heat ratio). The other variables in Eq. (1) include the inviscid flux vectors defined by,

$$\vec{F}_i = \begin{bmatrix} \rho \hat{u} \\ \rho u \hat{u} + \xi_x p \\ \rho v \hat{u} + \xi_y p \\ \rho w \hat{u} + \xi_z p \\ (\rho e + p) \hat{u} - \xi_t p \end{bmatrix} \quad \vec{G}_i = \begin{bmatrix} \rho \hat{v} \\ \rho u \hat{v} + \eta_x p \\ \rho v \hat{v} + \eta_y p \\ \rho w \hat{v} + \eta_z p \\ (\rho e + p) \hat{v} - \eta_t p \end{bmatrix} \quad \vec{H}_i = \begin{bmatrix} \rho \hat{w} \\ \rho u \hat{w} + \zeta_x p \\ \rho v \hat{w} + \zeta_y p \\ \rho w \hat{w} + \zeta_z p \\ (\rho e + p) \hat{w} - \zeta_t p \end{bmatrix} \quad (3)$$

Also, $J = \partial(\xi, \eta, \zeta, \tau) / \partial(x, y, z, t)$ is the transformation Jacobian, $\xi_x = (J^{-1}) \partial \xi / \partial x$ and similar terms define the metric quantities, and the transformed flow velocity components are given by,

$$\begin{aligned} \hat{u} &= \xi_t + \xi_x u + \xi_y v + \xi_z w \\ \hat{v} &= \eta_t + \eta_x u + \eta_y v + \eta_z w \\ \hat{w} &= \zeta_t + \zeta_x u + \zeta_y v + \zeta_z w \end{aligned}$$

The viscous flux vectors in Eq. (3) are defined, e.g., in Ref. [12], while S represents the source term which in the current work generates an incompressible turbulence upstream of the airfoil. All flow variables are normalized by their respective reference freestream values except for pressure which is nondimensionalized by $\rho_\infty u_\infty^2$. Note that the governing equations are represented in the original unfiltered form used unchanged in laminar, transitional or fully turbulent regions of the flow, with Ref. [13] providing further details on the code's employed Implicit LES (ILES) procedure in which a high-order low-pass filter operator is applied to the dependent variables during the solution process, in contrast to the standard LES addition of sub-grid stress (SGS) and heat flux terms. The resulting filter selectively damps the evolving poorly resolved high-frequency content of the solution.

The code employs a finite-difference approach to discretize the governing equations, with all the spatial derivatives obtained using the high-order compact-differencing schemes from Ref. [14]. For the airfoil flow computations in the current paper, a sixth-order scheme is used. At boundary points, higher-order one-sided formulas are utilized which retain the tridiagonal form of the scheme. In order to ensure that the Geometric Conservation Law (GCL) is satisfied, the time metric terms are evaluated employing the procedures described in detail in Ref. [11]. Finally, the time marching is accomplished by incorporating a second-order iterative, implicit approximately-factored procedure as described, e.g., in Ref. [13].

3 UPSTREAM SYNTHETIC TURBULENCE MODEL

The current study employs a *random flow generation* (RFG) model wherein a turbulent flow field is synthesized using a three-dimensional Fourier spectrum for perturbation flow velocity which matches prescribed energy spectrum with given turbulence integral scales. As described by Kraichnan [8] for isotropic turbulence and further elaborated by Smirnov et al [9] for general anisotropic case, the procedure to generate a synthetic turbulent field matching Gaussian spectral distribution involves several steps. First, for a given anisotropic velocity correlation tensor r_{ij} of a turbulent flow velocity field $\{u_i(x_j, t)\}_{i,j=1,\dots,3}$, the orthogonal transformation tensor a_{ij} is found that would diagonalize r_{ij} ,

$$\begin{aligned} a_{mi}a_{nj}r_{ij} &= \delta_{mn}c_{(n)}^2 \\ a_{ik}a_{kj} &= \delta_{ij}. \end{aligned} \tag{4}$$

Thus obtained scaling coefficients $c_{(n)}$ represent the three turbulent fluctuating velocity components in the coordinate system produced by the transformation tensor a_{ij} . Next, an intermediate randomly fluctuating velocity is constructed in the form,

$$\begin{aligned} v_i(\tilde{x}_j, \tilde{t}) &= \sqrt{\frac{2}{N}} \sum_{n=1}^N [p_i^n \cos(\tilde{k}_j^n \tilde{x}_j - \omega_n \tilde{t}) + q_i^n \sin(\tilde{k}_j^n \tilde{x}_j - \omega_n \tilde{t})], \\ \tilde{x}_j &= \frac{x_j}{L}, \quad \tilde{t} = \frac{t}{\tau}, \quad \tilde{k}_j^n = k_j^n \frac{L}{c_j}, \\ p_i^n &= \varepsilon_{ijm} \zeta_j^n k_m^n, \quad q_i^n = \varepsilon_{ijm} \xi_j^n k_m^n, \\ \zeta_j^n, \xi_j^n, \omega_n &\in N(0,1), \quad k_j^n \in N(0,1/2), \end{aligned} \tag{5}$$

where L and τ represent, respectively, the turbulent length and time scales which may be found by using the turbulence kinetic energy and dissipation rate from RANS simulations (e.g., in hybrid RANS/LES procedures [10]) or from an experiment. Random fluctuations are introduced using the permutation tensor ε_{ijm} in Eq. (5), and $N(M, \sigma)$ represents normal distribution with mean M and standard deviation σ . Note that thus generated wave numbers k_j^n and frequencies ω_n synthesize a sample of Gaussian turbulent energy spectrum,

$$E(k_j^n) = 16 \left(\frac{2}{\pi}\right)^{1/2} (k_j^n)^4 \exp(-2(k_j^n)^2) \tag{6}$$

Finally, the constructed fluctuating velocity in Eq. (5) is rescaled to obtain the required flowfield,

$$w_i(\tilde{x}_j, \tilde{t}) = c_i v_i(\tilde{x}_j, \tilde{t}), \tag{7}$$

$$u_i(x_j, t) = a_{ik} w_k(\tilde{x}_j, \tilde{t}). \tag{8}$$

In Eqs. (7-8), an additional rescaling is implemented to match the time and space scales of the numerical code and thus have the final turbulent flow velocity field correspond to the numerical turbulence-source implementation procedure outlined further below. Note that as shown by Smirnov et al [9], the above approach produces the velocity field which is divergence-free for homogeneous turbulence and nearly divergence-free for inhomogeneous

one.

In the numerical implementation of RFG model discussed in detail in Refs [5-6], the objective is to generate a three-dimensional, incompressible convected perturbation velocity field $\{u_i(x_j, t)\}_{i,j=1,2,3}$ from Eq. (8) by prescribing a momentum source in an arbitrary region of the computational domain upstream of a body. The procedure imposes such field described in terms of the Fourier spectrum containing superposition of harmonic functions,

$$u_i(x_j, t) = \sum_{n=1}^N (a_i^n \cos[k_j^n x_j - \omega_n t] + b_i^n \sin[k_j^n x_j - \omega_n t]). \quad (9)$$

Without loss of generality, the synthesized unsteady disturbance field is considered convected by a uniform mean flow u_∞ aligned with x_1 -direction so that the modal perturbation frequency ω_n is related to the wavenumber k_1^n by $\omega_n = u_\infty k_1^n$. Furthermore, the disturbance is assumed to be incompressible (divergence-free) which thus implies the following coupling between the modal amplitudes and wavenumbers:

$$a_i^n k_j^n = b_j^n k_i^n = 0 \quad (10)$$

Interactions between the perturbation modes and other waves are considered negligible. Thus, the momentum source terms S_i generating the disturbance velocity field in Eq. (9) should satisfy the following relationships,

$$\frac{\partial u_i}{\partial t} + U_\infty \frac{\partial u_i}{\partial x_1} = S_i \quad (11)$$

It can be shown that the solution for the momentum source terms imposed in the computational domain region with extent Δ_s in the mean flow convection direction (x_1) may be obtained in the form,

$$S_i(x_j, t) = \begin{cases} \sum_{n=1}^{\infty} \omega_n K_n g(x_1) (b_i^n \sin \sigma_n - a_i^n \cos \sigma_n) & \text{for } i = 1, \\ \sum_{n=1}^{\infty} U_\infty K_n g'(x_1) (b_i^n \cos \sigma_n + a_i^n \sin \sigma_n) & \text{for } i = 2, 3, \end{cases} \quad (12)$$

In Eq. (12), K_n is the constant,

$$K_n = \frac{\left(\frac{k_1^n}{2\pi} \Delta_s\right)^2 - 1}{\sin\left(\frac{k_1^n}{2} \Delta_s\right)} \quad (13)$$

$g(x_1)$ is the limiter function defined in this work as,

$$g(x_1) = \begin{cases} \frac{1}{2} \left(1 + \cos\left[\frac{2\pi}{\Delta_s}(x_1 - x_{1s})\right]\right) & \text{for } |x_1 - x_{1s}| \leq \frac{\Delta_s}{2} \\ 0 & \text{for } |x_1 - x_{1s}| > \frac{\Delta_s}{2} \end{cases}$$

$g'(x_1) = dg/dx_1$, and $\sigma_n = \omega_n t - k_1^n x_{1s} - k_2^n x_2 - k_3^n x_3$. The momentum source terms (12) are thus specified in an upstream region centered at $x_1 = x_{1s}$.

In the numerical procedure, for the synthesized field generated downstream of the source region, the energy spectra $E_i(x_j, f)$ corresponding to the disturbance velocity field (9) are

obtained with frequency resolution $\Delta f=1/T$ and $f_{\max}=1/2\Delta t$ based on data samples recorded with period T and sampling rate Δt .

To illustrate general features of the imposed and generated turbulent spectra and the corresponding aerodynamic responses, results of 2D studies conducted in Refs [5-6] are shown for SD7003 airfoil installed at an angle of attack $\alpha=8^\circ$ in the laminar flow with $M_\infty=0.1$ and $Re = \rho_\infty u_\infty c/\mu=10,000$. The upstream turbulence is synthesized with $N=100$ modes in the expansion (9) producing the Gaussian isotropic turbulent energy spectrum specified by Eq. (6). Selected input parameters include the non-dimensional turbulence length scale $L=0.035$ and turbulence intensity $I=0.35$ related to the diagonal velocity correlation tensor components in Eq. (4), $I = u_{rms,i} = \sqrt{r_{ii}}$ (all scaled according to the above-indicated code non-dimensionalization, with respect to the airfoil chord and far upstream flow velocity).

Fig. 3 shows the time snapshots of the vorticity contours illustrating the process of turbulence generation in the upstream source region and its downstream convection and interaction with airfoil.

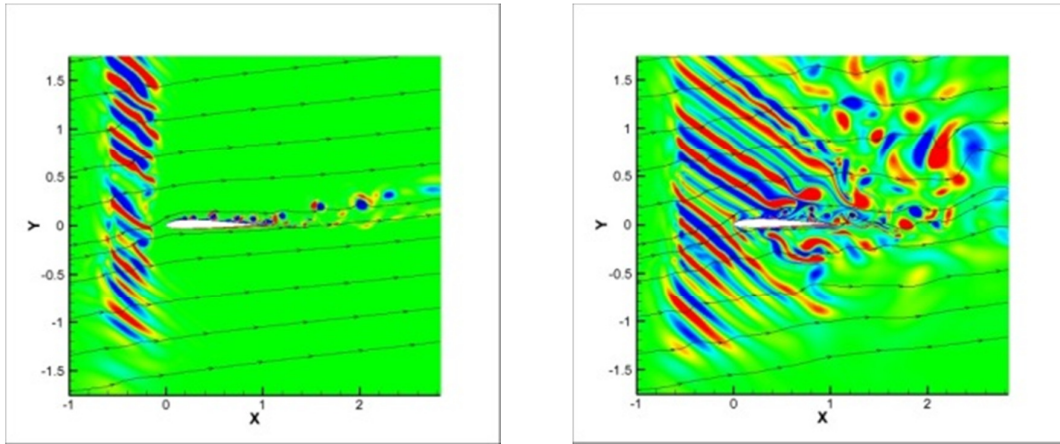


Figure 3: Vorticity and streamline contours illustrating generation and evolution of upstream turbulence, left to right: before and during interaction with airfoil.

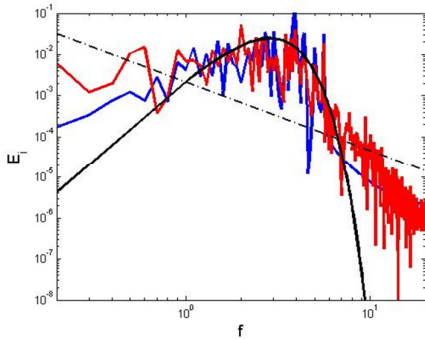


Figure 4: Comparison of prescribed (blue line), generated (red line) and targeted Gaussian (black line) upstream turbulent energy spectra.

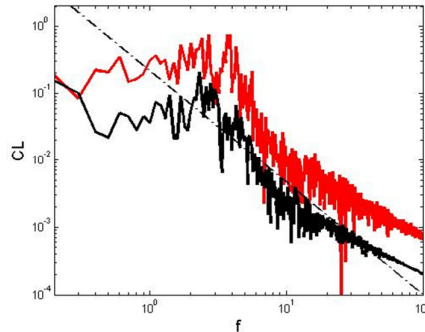


Figure 5: Lift spectra based on 2D turbulence-airfoil interaction over the period $T=10$ (red line) and the same period of airfoil quasi-steady response without upstream disturbance (black line).

Fig. 4 shows that the prescribed (synthesized) and source-generated turbulence spectra match well with each other and with the imposed Gaussian profile in the most energetic part of the spectrum. The resulting unsteady lift spectra in Fig. 5 closely follow the expected $(-5/3)$ rate of turbulent energy decay in the inertial subrange and confirm higher levels of the unsteady response induced by the high-intensity turbulence compared to the quasi-steady lift spectrum. Further details of these studies can be found in Refs [5-6].

4 TURBULENCE EFFECT ON FLOW-ACOUSTIC RESONANT INTERACTIONS

Refs [1-3] conducted a study of flow-acoustic resonant interactions in transitional NACA-0012 airfoil where the unsteady response signature was characterized by prominent acoustic frequency tones forming a dual ladder-type structure of tone frequency velocity dependence. This phenomenon was first observed in experiments by Paterson et al [4] whose results are shown in Fig. 2. Such acoustic signature is attributed to the feedback loop forming at certain flow conditions between the boundary-layer instability modes and the trailing-edge-scattered acoustic modes (Fig. 1). The proposed interpretation of Fig. 2 is that the rungs with frequency $f \sim U^{0.8 \dots 0.85}$ are related to the amplified instability-wave trailing-edge scattering, and the effectively produced vortex shedding corresponds to the dominant frequencies of each rung scaled with $f_s \sim U^{1.5}$. Experimental and numerical studies of Refs [1-3] addressed both the spectral responses and the boundary-layer statistical moments characteristic of the observed phenomena, with the latter focusing on the effect of laminar separation bubble on instability amplification that ensures the sustained feedback loop. Furthermore, the effect of a *weak* upstream turbulence on radiated sound was examined experimentally using an upstream turbulence grid installed in an anechoic wind tunnel facility. For the NACA-0012 airfoil installed at $\alpha=5^\circ$ in a low-speed flow with moderate Reynolds number, the main effect of the upstream turbulence was suppression of all tones associated with acoustic feedback and the 0.85-power ladder-type structure. At the same time, a broadband hump with 1.5-power law dependence was evident without distinct tonal peaks.

To study the effect of upstream turbulence on the feedback-loop interactions in transitional boundary layers, the current work extends the previous numerical analyses of Refs [1-3] by employing the turbulence model described in Section 3.

We consider the experimental case with NACA-0012 airfoil with the chord $c=0.1\text{m}$ installed at the geometric angle of attack $\alpha=5^\circ$. In the numerical analysis, the calculations are performed for $\alpha=2^\circ$ to account for the wind-tunnel correction, as specified in Refs [1-3]. The selected case corresponds to the mean flow velocity of 25 m/s, with the analysis conducted for $Re=180,000$ closely representing the experimental conditions. A sectional 1281×789 O-grid is employed.

The computations employ a physical time step of 0.3625×10^{-6} sec corresponding to the code non-dimensionalized time step of 9×10^{-4} . In the numerical experiments, the upstream turbulence, prescribed with non-dimensional length scale $L=0.035$ and intensities $I=0.001, 0.008$ and 0.07 , is continuously generated in order to collect sufficient statistical data for the spectral analyses. The steady-state flow condition is first reached after marching for 200,000 steps. The pressure signals are then recorded for over 720,000 steps, hence for the baseline set-up collecting the data sample for 0.26 sec with the sampling rate of 62.7 kHz and achieving the frequency resolution of $\Delta f=3.83\text{Hz}$.

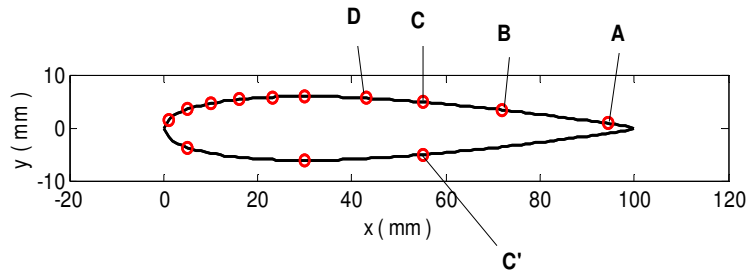


Figure 6: Locations of RMPs on NACA-0012 mock-up (red symbols) and reference points for the analysis of wall-pressure fluctuations.

Fig. 6 illustrates positions of the remote microphone probes (RMPs) for the unsteady pressure measurements in the experiment at which the statistical data is also collected in the numerical analyses.

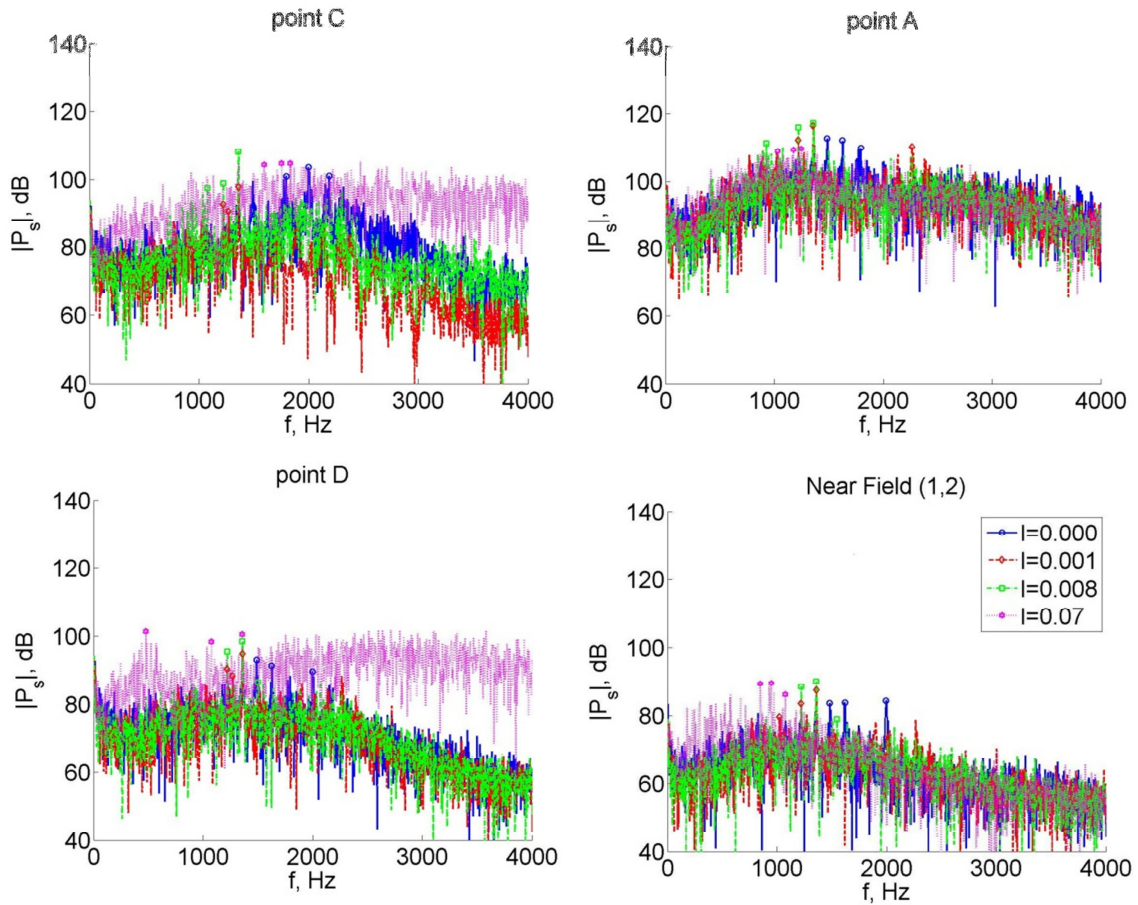


Figure 7: Comparison of pressure spectra at selected monitor points for uniform and turbulent inflows .

Results in Fig. 7 compare the pressure spectra at selected points on the surface and in the near field (2 chords above the trailing edge), for the cases of the upstream turbulence with $I=0.001$, 0.008 and 0.07 vs. the benchmark case of the uniform upstream flow. Shifts in the (marked) dominant frequencies are notable, and it is also evident that the resonant interactions are not eliminated as a result of the impinging low-intensity turbulence with $I=0.001$ and 0.008 . On the contrary, more prominent tones are observed for those two cases on the suction side near the separation area (Point C) compared to the case with the uniform upstream flow. For much higher turbulence intensity ($I=0.07$), the results indicate a suppression of prominent tones in the surface spectra downstream of point D, with much higher broadband levels noticed at the airfoil mid-chord on the suction side. Note that a high-fidelity analysis of the airfoil unsteady response in such case (characterized by the developed turbulent boundary layer) would warrant fully 3D ILES simulations, with the corresponding results to be reported in the subsequent work.

Fig. 8 illustrates the mean and RMS pressure distributions on the airfoil surface obtained for the turbulent intensities $I=0.008$ and 0.07 , in comparison with those for the benchmark uniform upstream flow case. For the latter, the mean pressure distribution has been previously validated against experimental data and appears close to the cases with upstream turbulence, except near the separation region. The differences are more apparent for RMS pressure, with the low-turbulence ($I=0.008$) results generally close to the benchmark ones, in contrast to the case with $I=0.07$ for which the strong leading-edge peaks are followed by the overall much higher RMS levels on the suction side. Eventually, a match for all three cases is observed in the aft portion of the airfoil, with sustained similar levels shown on both airfoil sides. Note that as indicated in Refs [2-3], 3D ILES results for the benchmark case rather reveal a rapid decrease of RMS pressure amplitudes towards the trailing edge after reaching the peak levels, which appears to be related to the spanwise flow redistribution. However, the peak RMS levels were similar in 2D and 3D computations.

The sensitivity of the location of the separated regions is deduced from the surface distributions of the skin friction coefficient shown in Fig. 9. In the previous 2D simulations [1-3], the separated zones were shown to be localized on the suction side, with their positions sensitive to the Reynolds number. The location of the separated region is critical since it can be directly linked to the amplification of the instability waves and thus the sustainment of the acoustic feedback process. In 2D analysis for the benchmark case with the uniform upstream flow, the separated regions on the suction side form between $x=0.5c$ and $x=0.75c$ starting with a very thin separated layer and followed by a near-reattachment point at $x=0.67$ and a rather short laminar bubble. For the low-intensity turbulence case, such separation area has moved upstream and is barely present near the mid-chord location on the suction side. It completely vanishes for the case with $I=0.07$, which thus may explain the disappearance of the acoustic feedback on the suction side and clearly defined spectral tones in Fig 7. Along the pressure side (the bottom plots in Fig. 9), the separation areas are reached very close to the trailing edge and appear similar in all three cases. Such areas are characterized by the rapid growth of RMS pressure and may sustain the acoustic feedback process on the pressure side even in the case with $I=0.07$, which may explain the near-field peaks observed for this case in Fig.7.

In Fig. 10, the boundary-layer dynamics on the suction side is illustrated by comparing variations of the mean and RMS of the tangential velocity component V_t obtained for the turbulent case with $I=0.008$ (left plots) vs. the benchmark case (right plots). The results are

shown for seven points between $x=0.7$ and $x=0.95$, with the corresponding color for each plot indicated in the legend in Fig. 10. The results appear very similar for the two cases. Fig. 11 further compares evolutions of RMS of V_t obtained for the two turbulent cases (with $I=0.008$ and 0.07) on both the suction (top plots) and pressure (bottom plots) sides, and confirms much more pronounced differences in the boundary-layer dynamics for these two cases.

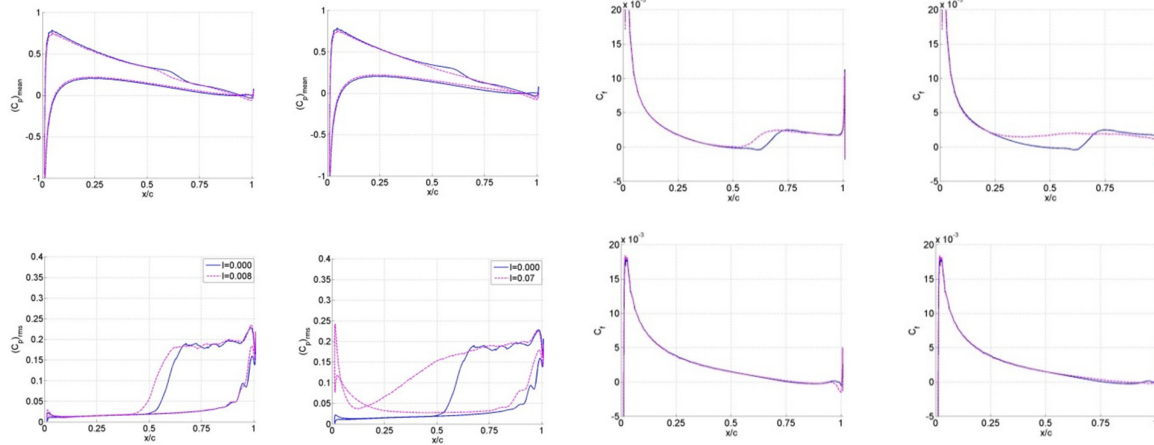


Figure 8: Surface mean (top) and RMS (bottom) pressure distributions for uniform (blue lines) vs turbulent upstream flow (red lines) with $I=0.008$ (left plots) and $I=0.07$ (right plots).

Figure 9: Skin friction coefficient on suction (top) and pressure (bottom) airfoil sides for uniform (blue lines) vs turbulent upstream flow (red lines) with $I=0.008$ (left plots) and $I=0.07$ (right plots).

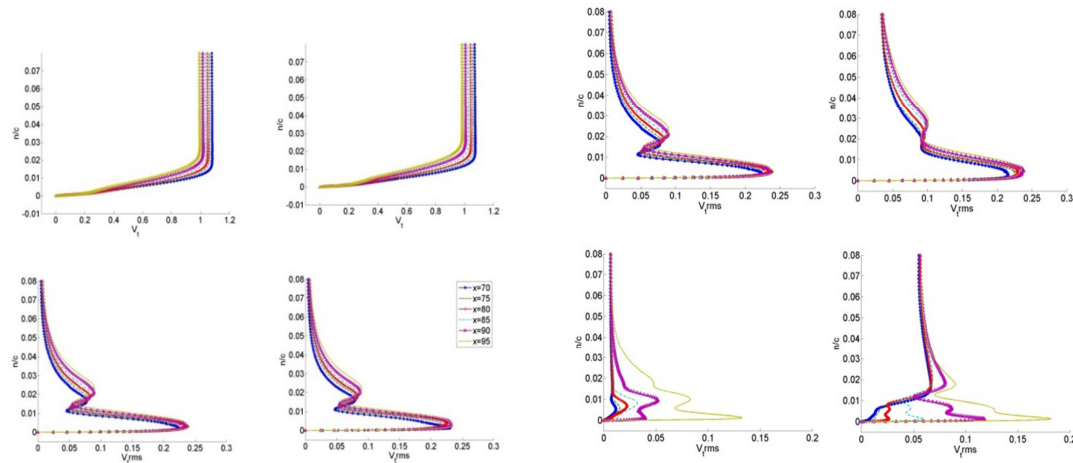


Figure 10: Mean (top) and RMS (bottom) tangential velocity boundary-layer profiles along the airfoil suction surface for turbulent upstream flow with $I=0.008$ (left plots) vs. uniform upstream flow (right plots).

Figure 11: RMS tangential velocity boundary-layer profiles along the airfoil suction (top) and pressure (bottom) sides for turbulent upstream flows with $I=0.008$ (left plots) and $I=0.07$ (right plots) (plot legends and the same as in Fig. 10).

Finally, Fig. 12 quantifies the overall growth of the boundary-layer velocity fluctuations

by showing the predicted evolutions of RMS maxima for the tangential velocity components V_i evaluated across the boundary layers on both airfoil sides. Such evolution may be indicative of the instability growth rate when the acoustic feedback process is sustained (note also a close correlation with Fig. 8 for RMS pressure). Indeed, for the uniform and low-turbulence upstream flow conditions, the rapid growths of the instability amplitudes on the suction side are clearly associated with the formed laminar separation zones and the corresponding transition from viscous to inviscid instability growth mechanism (with the latter characterized by much higher amplification rates). The saturation of the instability growth appears to be linked to the flow reattachment locations. For the high-intensity turbulence case with $I=0.07$, much higher RMS levels are associated with fully turbulent flow conditions on the suction side where the laminar instabilities and the feedback-loop process appear to be fully suppressed. In all the considered cases, the pressure side may sustain the flow-acoustic resonant interactions associated with the rapid instability growth through the separation regions forming close to the trailing edge.

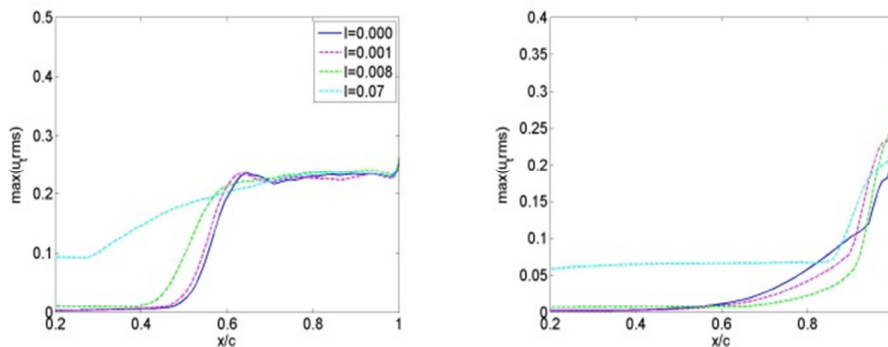


Figure 12: Evolution of $\text{Max}(V_{i,RMS})$ along suction (left) and pressure (right) sides for turbulent vs. uniform upstream flow conditions.

5 CONCLUSIONS

A novel approach to introduce a synthetic turbulent field in a source region upstream of an airfoil was employed to investigate the effect of the upstream turbulence intensity of flow-acoustic resonant interactions in transitional airfoils. High-accuracy numerical 2D simulations were conducted for NACA-0012 airfoil installed at $\alpha=2^\circ$ in a flow with mean velocity of 25 m/s and $Re=180,000$. In the numerical experiments, the upstream turbulence with intensities $I=0.001$, 0.008 and 0.07 was continuously generated in order to collect sufficient statistical data.

Comparison of the pressure spectra for the different intensity levels against the benchmark case of the uniform upstream flow was carried out at selected points on the airfoil surface and in the near field. Results indicated notable shifts in the dominant frequencies of the unsteady airfoil response. Prominent tones were observed for the low-intensity cases ($I=0.001$ and 0.008) on the suction side all the way to trailing edge and in the near field. For the high turbulence intensity ($I=0.07$), the results indicated a suppression of prominent tones in the surface spectra downstream of the mid-chord location on the suction side, with much higher broadband levels. A high-fidelity 3D ILES analysis of the airfoil unsteady response may be

warranted in such case and will be reported in the subsequent work.

The analysis of the boundary-layer statistical moments indicated that for the uniform and low-turbulence upstream flow conditions, the rapid growth of the instability amplitudes on the suction side was associated with the formation of the laminar separation zones and the corresponding switch from the viscous to inviscid instability growth mechanism characterized by much higher amplification rates. The growth saturation was linked to the flow reattachment occurring without subsequent turbulence transition, thus enabling preservation of the coherent instability modes and the feedback mechanism. For the high-intensity turbulence case with $I=0.07$, the much higher RMS levels were associated with the fully turbulent flow conditions reached on the suction side where the laminar instabilities and the feedback-loop process appeared to be suppressed. In all the considered cases, the pressure side sustained the flow-acoustic resonant interactions associated with the rapid instability growth through the separation regions forming close to the trailing edge.

REFERENCES

- [1] V.V. Golubev, L. Nguyen, M. Roger and M.R. Visbal, On Interaction of Airfoil Leading and Trailing Edge Noise Sources in Turbulent Flow. *AIAA Paper 2011-2859*, 2011.
- [2] V.V. Golubev, L. Nguyen, M. Roger and M.R. Visbal, High-Accuracy Simulations of Flow-Acoustic Resonant Interactions in Airfoil Transitional Boundary Layers. *AIAA Paper 2012-2136*, 2012.
- [3] V.V. Golubev, L. Nguyen, R. Mankbadi, M. Roger, and M.R. Visbal, Acoustic Feedback-Loop Interactions in Transitional Airfoils, *AIAA Paper 2013-2111*, 2013.
- [4] R. Paterson, P. Vogt, M. Fink, and C. Munch, Vortex Noise of Isolated Airfoils. *J. Aircraft*. 10 (1973) 296-302.
- [5] V.V. Golubev, J. Brodnick, L. Nguyen and M.R. Visbal, New Approach to Modeling Airfoil Interaction with Upstream Turbulence. *AIAA Paper 2011-3899*, 2011.
- [6] V.V. Golubev, J. Brodnick, L. Nguyen and M.R. Visbal, High-Fidelity Simulations of Airfoil Interaction with Upstream Turbulence. *AIAA Paper 2012-3071*, 2012.
- [7] V.V. Golubev, B.D. Dreyer, M.R. Visbal, and N.V. Golubev, High-Accuracy Viscous Simulation of Gust Interaction with Stationary and Pitching Wing Sections. *AIAA Paper 2009-0011*, 2009.
- [8] R.H. Kraichnan, Diffusion by a Random Velocity Field. *Physics of Fluids*, 13(1970), 22-31.
- [9] R. Smirnov, S. Shi, and I. Celik, Random Flow Generation Technique for Large Eddy Simulations and Particle-Dynamics Modeling. *Journal of Fluids Engineering*, 123 (2001), 359-371.
- [10] P. Batten, U. Goldberg, and S. Chakravarthy, Interfacing Statistical Turbulence Closures with Large-Eddy Simulation. *AIAA Journal*, 42 (2004), No.3, 485-492.
- [11] M.R. Visbal and D.V. Gaitonde, On the Use of High-Order Finite-Difference Schemes on Curvilinear and Deforming Meshes. *J. Computational Physics*, 181 (2002) 155–185.
- [12] D.A. Anderson, J.C. Tannehill, and R.H. Pletcher, *Computational Fluid Mechanics and Heat Transfer*, McGraw-Hill Book Company (1984).
- [13] M.R. Visbal, P.E. Morgan, and D.P. Rizzetta, An Implicit LES Approach Based on High-Order Compact Differencing and Filtering Schemes. *AIAA Paper 2003-4098* (2003).
- [14] S.K. Lele, Compact Finite Difference Schemes with Spectral-like Resolution. *J. Computational Physics*, 103 (1992) 16–42.